Available online at www.sciencedirect.com
ScienceDirect
Nuclear Physics A 00 (2022) 1–??
Nuclear Physics A

β-decay half-lives and nuclear structure of exotic proton-rich waiting point nuclei under rp-process conditions

Jameel-Un Nabi[1] and Mahmut Böyükata[2]

[1]*Faculty of Engineering Sciences, GIK Institute of Engineering Sciences and Technology, Topi 23640, Swabi, Khyber Pakhtunkhwa, Pakistan*

[2]*Department of Elementary Science Education, Faculty of Education, Çanakkele Onsekiz Mart University, TR-17100, Çanakkele, Turkey*

Abstract

We investigate even-even nuclei in the $A \sim 70$ mass region within the framework of the proton-neutron quasi-particle random phase approximation (pn-QRPA) and the interacting boson model-1 (IBM-1). Our work includes calculation of the energy spectra and the potential energy surfaces $V(\beta, \gamma)$ of Zn, Ge, Se, Kr and Sr nuclei with the same proton and neutron number, $N = Z$. The parametrization of the IBM-1 Hamiltonian was performed for the calculation of the energy levels in the ground state bands. Geometric shape of the nuclei was predicted by plotting the potential energy surfaces $V(\beta, \gamma)$ obtained from the IBM-1 Hamiltonian in the classical limit. The pn-QRPA model was later used to compute half-lives of the neutron-deficient nuclei which were found to be in very good agreement with the measured ones. The pn-QRPA model was also used to calculate the Gamow-Teller strength distributions and was found to be in decent agreement with the measured data. We further calculate the electron capture and positron decay rates for these $N = Z$ waiting point (WP) nuclei in the stellar environment employing the pn-QRPA model. For the rp-process conditions, our total weak rates are within a factor two compared with the Skyrme HF+BCS+QRPA calculation. All calculated electron capture rates are comparable to the competing positron decay rates under rp-process conditions. Our study confirms the finding that electron capture rates form an integral part of the weak rates under rp-process conditions and should not be neglected in the nuclear network calculations.

Keywords: β-decay half-lives, waiting point nuclei, rp-process, IBM, pn-QRPA, Gamow-Teller strength distribution, potential energy surfaces, electron capture.
PACS: 21.10.-k, 21.60.Cs, 21.60.Jz, 21.60.Ev, 21.60.Fw, 23.40.-s, 26.20.Np, 26.30.Ca, 26.30.Jk, 26.50.+x, 27.50.+e

1. Introduction

Modeling and simulation of the explosive phenomena involve the knowledge of the properties of the exotic nuclei. X-ray bursts (see e.g. [1, 2]) are generated by a thermonuclear runaway in an hydrogen-rich environment where an accreting neutron star is fed from a binary partner (usually a red giant). The ignition starts as soon as the temperature T and the density ρ in the accreted disk due to mass transfer become sufficiently high to permit a breakout from the hot CNO cycle. Stellar temperatures in the vicinity of $T = 1 - 3$ GK and densities in the range $\rho = 10^6 - 10^7$ gm.cm^{-3} are believed to facilitate the development of the nucleosynthsis along the proton-rich side via rapid proton capture (rp) process (see e.g. [1, 3]). Studies (e.g. [4]) have pointed toward extreme hydrogen burning where at sufficiently high temperature ($T_9 \leq 0.8$K) and density conditions ($\rho \geq 10^4$ gcm^{-3}), depending on the time scale of the explosive event, the rp- and the αp-processes reaction path may well proceed beyond mass A =64 and Z = 32. The proton capture processes are orders of the magnitude faster than β-decays or any other competing processes. Schatz and collaborators

[5] found out that the rp-process is responsible for producing heavy proton-rich nuclei reaching mass number 100 that ends in a closed SnSbTe cycle. It also explained the luminosity and the energy profiles present in the X-ray bursts.

The reaction path for rp-process follows a series of rapid proton capture reactions producing heavy nuclei. The process culminates when a radioactive element is produced and later proceeds through a β-decay (double proton capture are less probable). The reaction flow then has to wait for a relatively slower β-decay and this nucleus is termed as a waiting point (WP) nucleus. Typical time scale of the rp-process is $\sim 100\ s$. Half-lives of the WP nuclei is roughly of the same order and hence determine the time scale of the nucleosynthesis process and isotopic abundances. Consequently, weak-interaction mediated stellar rates of the neutron-deficient medium-mass nuclei play a crucial role in a better understanding of the rp-process. Authors in Ref. [1] claimed that important parameters for a successful rp-process nucleosynthesis calculation include nuclear masses, nuclear deformations (specially in the regime A = 60 – 80 because of the wide variety of the nuclear shapes displayed in the region) and finally a reliable calculation of the stellar electron capture and β-decay rates of the WP nuclei along a given reaction path since they determine time structure and abundance patterns.

New generation radioactive ion-beam facilities (e.g. FAIR (Germany), FRIB (USA) and FRIB (Japan)) are expected to reveal some exciting facts about exotic nuclei but the current status is that majority of them are not well explored. Consequently, astrophysical simulations of the violent and explosive events must be built on nuclear-model predictions which in turn need to be microscopic and reliable. We attempt first to calculate nuclear shape of the WP nuclei using a microscopic model. In this article, the calculation of the interacting boson model (IBM) [6, 7, 8, 9] is performed for the low-lying collective levels and the prediction of geometric shape of the $N = Z$ WP nuclei. The investigation of the nuclear properties of nuclei in various region of the nuclear chart within IBM model is still one of the hot subjects. Many experimental data of nuclei in the isotopic (or isotonic) chain have been compared with the IBM calculations (for recent works, see Refs. [10, 11, 12, 13]). The prediction of the geometric type of nuclei with the corresponding potential energy surface (PES) of the IBM model is also favorite subject as seen recently work in Refs. [14, 15, 16, 17, 18, 19, 20].

For the $A \sim 70$ mass region, the structure of the energy spectra of ^{64}Ge isotope with neighbors up to ^{78}Ge was investigated within the extended IBM model [21] and a transition from the mixture of $SU(3)$, $O(6)$, $U(5)$ symmetries (mixture of prolate, γ-unstable, spherical shapes) to $O(6)$ and $U(5)$ (mixture of γ-unstable, spherical shapes) and then finally $U(S)$ symmetry (spherical shape) appear along to isotopic chain of even-even $^{64-78}$Ge. The positive-parity bands of the even-even $^{72-84}$Kr isotopes were studied within the framework of the IBM-2 model [22] by taking in to account the $U(5)$ symmetry of the model as a starting point of the investigation.

For the potential energy surfaces (PESs), Hartree-Fock-Bogoliubov (HFB) model have been applied to this region as follows: the PESs of the ^{64}Ge, ^{68}Se, ^{72}Kr, ^{76}Sr, ^{80}Zr and ^{84}Mo were calculated within the HFB model using the Skyrme interaction [23] and in this work the shape transition changes from triaxial for ^{64}Ge, oblate for ^{68}Se, ^{72}Kr, large prolate for ^{76}Sr, ^{80}Zr, to spherical for ^{84}Mo. The PESs of $^{64-72}$Ge were calculated with the HFB model plus the GognyD1S interaction [24] and the results indicate that ^{64}Ge is rigid triaxial, ^{66}Ge is γ-unstable, $^{68-72}$Ge isotopes are soft triaxial. The solutions of the HFB model were applied to ^{68}Se and ^{72}Kr nuclei [25] to describe the oblate-prolate shape coexistence phenomena in these nuclei by using the pairing-plus-quadrupole (P+Q) interaction. The PESs of the $^{72-76}$Kr were performed within the HFB method by using the D1S interaction and the minima for ^{74,76}Kr are located at axial deformed while the absolute minimum is found at oblate deformation for ^{72}Kr [26]. The oblate-prolate shape coexistence in proton-rich ^{68,70,72}Se is investigated within the constrained HFB plus the local QRPA (CHFB+LQRPA) equation by using the P+Q interaction [27]. The PESs of the even-even Ni, Zn, Ge, Se, Kr, Sr, Zr, Mo, Ru, Pd, Cd, and Sn nuclei around the $N = Z$ line cover a whole proton shell ranging from $Z = 28$ up to $Z = 50$ have been worked within the HF + BCS calculations plus the Skyrme force SLy4 [28]. Both the lighter and heavier nuclei close to $Z = 28$ and $Z = 50$ tend to be spherical. The deformed shapes appear around the mid shell nuclei in this work.

The main purpose of this work is to investigate some nuclear structure properties like energy levels, B(E2) values, PES and to calculate half- lives and stellar weak rates of the WP nuclei. The energy levels in the ground state band of the nuclei in $N = Z$ line were calculated to fit essential IBM Hamiltonian parameters. Later the potential energy surfaces of each nuclei were plotted to get the deformation parameter β. The nuclear model chosen to calculate terrestrial and stellar weak decay rates is the proton-neutron quasiparticle random phase approximation (pn-QRPA) which has a proven track-record for the calculation of electron capture and β-decay rates. Half-lives of the β^- decays were calculated systematically for about 6000 neutron-rich nuclei between the beta stability line and the neutron drip line using the pn-QRPA model [29]. Similarly half-lives for β^+/electron capture decays for neutron-deficient nuclei

with atomic numbers Z = 10 - 108 were calculated up to the proton drip line for more than 2000 nuclei using the same model [30]. These microscopic calculations gave a remarkably good agreement with the then existing experimental data (within a factor of two for more than 90% (73%) of nuclei with experimental half-lives shorter than 1 s for β^- (β^+/EC) decays). Later Nabi and Klapdor-Kleingrothaus reported the calculation of the weak-interaction rates for more than 700 nuclei with A = 18 to 100 in stellar environment using the same nuclear model [31].

The paper is designed as follows: The IBM model is introduced and its Hamiltonian with formalism of the potential energy surface are presented in Section 2. The pn-QRPA model and formalism for calculation of stellar rates are discussed in Section 3. We discuss our calculation and compare with measured data and previous calculations in Section 4. Conclusions are finally stated in Section 5.

2. The interacting boson model (IBM)

The interacting boson model (IBM) of Arima and Iachello [6, 7, 8, 9], originally applicable to even-even nuclei, is quite successful to describe the collective properties of medium mass and heavy nuclei. The necessary components of the IBM are the s and the d bosons with angular momenta zero and two, respectively. The IBM model is also connected to the nuclear shell model [32] by the realization that the s and d bosons can be interpreted as correlated Cooper pairs formed by two valence nucleons in the shell coupled to angular momenta $L = 0$ and $L = 2$. The simplest version of the model, making no distinction between proton and neutron bosons, is called as sd-IBM as well as IBM-1 model. The extended version of model that separates the proton and neutron bosons, is normally referred to as proton-neutron (pn)-IBM or IBM-2 [33, 34, 35]. The algebraic IBM-1 model is defined by a six-dimensional space because of the s ($L = 0$, $\mu = 0$) and the d ($L = 2$, $-2 \leq \mu \leq 2$) bosons. The model needs a description of the $U(6)$ group structure. This group presents three possible dynamical symmetries, labeled by $U(5)$, $SU(3)$ and $O(6)$ limits, appearing in the following group chains:

$U(6) \supset U(5) \supset O(5) \supset O(3)$

$U(6) \supset SU(3) \supset O(3)$

$U(6) \supset O(6) \supset O(5) \supset O(3)$.

Each of the three standard symmetries are related to the geometrical shape of the nuclei; (i) the $U(5)$ limit corresponds to the spherical, (ii) $SU(3)$ limit describes the axially deformed nuclei and (iii) $O(6)$ limit defines γ-unstable (asymmetric deformed) nuclei. One of the characteristic clue for each symmetries is the energy ratio $R_{4/2} = E(4^+)/E(2^+)$ in the ground state band. This ratio is 2.0 for the spherical, 2.5 for γ-unstable and 3.33 for the axially deformed nuclei.

2.1. The IBM-1 Hamiltonian

The IBM-1 model describes a system of the s and the d bosons interactions, and therefore, the general IBM-1 Hamiltonian includes combinations of the operators s, $s^\dagger$, d, $d^\dagger$ [7, 8, 9]. This Hamiltonian has six interactions in total, *1* single-particle energy and *5* two-body interactions between the bosons. These interactions are used as free parameters in the Hamiltonian and these parameters must be fitted to the experimental data. The most general Hamiltonian can also be written as the sum of the quadratic Casimir operators of the subgroups of the complete $U(6)$ group chain. However, the most commonly used type of the IBM-1 Hamiltonian, also used in this work, is called multipole expansion in terms of the six parameters given in the following form [36];

$$\hat{H} = \epsilon\, \hat{n}_d + a_0\, \hat{P}_+ \cdot \hat{P}_- + a_1\, \hat{L} \cdot \hat{L} + a_2\, \hat{Q} \cdot \hat{Q} + a_3\, \hat{T}_3 \cdot \hat{T}_3 + a_4\, \hat{T}_4 \cdot \hat{T}_4, \tag{1}$$

where $\hat{n}_d$ is the boson-number operator, $\hat{P}_+$ is the boson pairing operator, $\hat{L}$ is angular momentum operator, $\hat{Q}$ is quadrupole operator, and $\hat{T}_3$, $\hat{T}_4$ are the octupole, hexadecapole operators, respectively and defined as

$$\begin{aligned}
\hat{n}_d &= \sqrt{5}[d^\dagger \times \tilde{d}]_0^{(0)}, \\
\hat{P}_+ &= [s^\dagger \times s^\dagger + \sqrt{5}\, d^\dagger \times d^\dagger]_0^{(0)}, \qquad \hat{P}_- = \left(\hat{P}_+\right)^\dagger, \\
\hat{L} &= \sqrt{10}[d^\dagger \times \tilde{d}]^{(1)}, \\
\hat{Q} &= [d^\dagger \times \tilde{s} + s^\dagger \times \tilde{d}]^{(2)} + \overline{\chi}[d^\dagger \times \tilde{d}]^{(2)}, \\
\hat{T}_\ell &= [d^\dagger \times \tilde{d}]^{(\ell)}, \qquad\qquad \ell = 3, 4.
\end{aligned} \tag{2}$$

Eq. (1) has the advantage that the constants have been used to describe the properties of a single nucleus by fitting to experimental nuclear spectra [37]. The combination of the linear and the quadratic operators of the $U(6)$ group and its subgroups; $U(5)$, $SU(3)$, $O(6)$, $O(5)$, $O(3)$ can be written in terms of the operators of the multipole form of the IBM-1 Hamiltonian given in Eqs. (1) and (2). The connections of the parameters for each forms of the Hamiltonian can be reviewed in detail from Ref. [36]. In addition to the energy levels, the electric quadrupole transition rates can also be calculated in the IBM-1 model by using the quadrupole transition operator, $\hat{T}(\mathrm{E2}) = e_{\mathrm{b}} \cdot \hat{Q}$. Here, e_{b} is the boson effective charge, $\hat{Q}$ is the quadrupole operator and has the same role as shown in Eq. (2).

2.2. The geometry: The potential energy surface

The investigation of the geometric character of the nucleus is one of the interesting subjects in nuclear physics. The IBM model has a relationship with the geometric model of Bohr and Mottelson [38]. Within the IBM model, the geometric shape of the nuclei can be also visualized by plotting the potential energy surface in terms of the deformation parameters β and γ. This potential energy surface $V(\beta, \gamma)$ can be obtained from the IBM-1 Hamiltonian in the classical limit [39, 40, 41, 42] as

$$V(\beta,\gamma) = \epsilon N \frac{\beta^2}{1+\beta^2} + a_1 6N \frac{\beta^2}{1+\beta^2} + a_2 N \left[\frac{5 + (1+\overline{\chi}^2)\beta^2}{1+\beta^2} + (N-1) \frac{\left(\frac{2\overline{\chi}^2\beta^4}{7} + 4\sqrt{\frac{2}{7}}\overline{\chi}\beta^3\cos(3\gamma) + 4\beta^2 \right)}{(1+\beta^2)^2} \right]$$
$$+ a_0 \frac{N(N-1)}{4} \frac{1-\beta^2}{1+\beta^2} + a_3 7N \frac{(5+\overline{\chi}^2)}{5} \frac{\beta^2}{1+\beta^2} + a_4 N \left[\frac{9}{5} \frac{\beta^2}{1+\beta^2} + \frac{18}{35}(N-1) \frac{\beta^4}{(1+\beta^2)^2} \right]. \quad (3)$$

This formula is reproduced for the most general IBM-1 Hamiltonian (1). Both Eqs (1) and (3) include common parameters, except for the deformation parameters. Here, N is number of the bosons and $\overline{\chi}$ belongs to the quadrupole operator given in Eq. (2). The β and γ variables play the same role as in the geometric collective model (GCM). For spherical nuclei, $\beta = 0$, $\gamma = 0^\circ$ and for the deformed nuclei; $\beta \neq 0$ and $\gamma = 0^\circ, 30^\circ, 60^\circ$ for prolate, triaxial, and oblate shapes, respectively. However, the classical limit for the Hamiltonian of each limit: $U(5)$, $U(5)$, $U(5)$, can also be derived as shown in Refs. [39, 43].

3. The pn-QRPA formalism and stellar weak rates

In our pn-QRPA model, single particle energies and wave functions were calculated using the Nilsson model [44], as it takes into account nuclear deformation. Pairing correlation was treated in the BCS approximation. The proton-neutron residual interactions occur through two channels, namely as particle-hole and particle-particle interactions. These interactions were given separable form and were characterized by two interaction constants χ and κ, respectively. We wanted to incorporate nuclear deformation parameter (β) from the IBM-1 model. However β in IBM model plays a slightly different role than β does in different geometric models. Whereas in the IBM β describes the quadrupole mixing of only the $2N$ valence nucleons (the remaining $A - 2N$ are in a spherical core), β in geometrical models refers to the deformation of all A nucleons [42]. Then the bosons in the IBM approximate fermion pairs. So naturally the properties of the nucleus will depend on the structure of these pairs. The deformations in the two models are connected by $\beta_{geom} \lesssim 1.18(2N/A)\beta_{IBM}$ as explained in detail in Ref. [42]. Nomura and collaborators [45] studied this relationship and tried to relate the IBM parameters with the microscopic selfconsistent mean-field calculations. They found that the β parameters in the two models were related roughly within a factor 3–5 [45]. It was apparent that linking the two deformation is not so simple. The deformation parameter was argued to be one of the most important parameters in pn-QRPA calculations [29, 46] and therefore we decided to use the β parameter from the relativistic mean-field calculation by Lalazissis and collaborators [47]. Calculated β parameters within the IBM-1 model and relativistic mean-field model are shown in Table 1. The particle-hole and particle-particle interactions strength parameters, χ and κ, are regarded as the two most important model parameters in the pn-QRPA theory (see Refs. [29, 30]). In this work, κ was fixed at 0.1 MeV. The particle-hole interaction parameter χ is known to affect the position of the Gamow-Teller giant resonance and was set using a $1/A$ dependence [30]. We were able to deduce a value of $4.2/A$ as the optimum value of χ which best reproduced the experimental half-lives [48] using the deformation parameter

from [47]. It is to be noted that a previous pn-QRPA calculation [49] used different values for χ and κ for the case of ^{72}Kr and ^{76}Sr because in that calculation deformation parameter was used from [50]. For further discussion on choice of these two parameters we refer to [30] and references therein. Nuclear masses and Q-values required for the calculation were taken from the recent atomic mass evaluation AME2012 [48].

The electron capture (ec) and the positron decay (pd) rates of a transition from the i^{th} state of the parent to the j^{th} state of the daughter nucleus are given by

$$\lambda_{ij}^{ec(pd)} = \left[\frac{\ln 2}{D}\right]\left[B(F)_{ij} + \left(g_A/g_V\right)^2 B(GT)_{ij}\right]\left[f_{ij}^{ec(pd)}(T,\rho,E_f)\right]. \tag{4}$$

The value of D was taken to be 6295s [51]. B(F) and B(GT) are reduced transition probabilities of the Fermi and Gamow-Teller (GT) transitions, respectively,

$$B(F)_{ij} = \frac{1}{2J_i+1} \mid< j \parallel \sum_k t_\pm^k \parallel i >\mid^2 . \tag{5}$$

$$B(GT)_{ij} = \frac{1}{2J_i+1} \mid< j \parallel \sum_k t_\pm^k \vec{\sigma}^k \parallel i >\mid^2 . \tag{6}$$

Here $\vec{\sigma}^k$ is the spin operator and $t_\pm^k$ stands for the isospin raising and lowering operator with (g_A/g_V) = -1.254 [52]. Details of the calculation of the reduced transition probabilities can be found in Ref. [53, 54]. We used a quenching factor of 0.6 in our calculation as normally employed in most shell model and QRPA calculations of the weak rates.

The $f_{ij}^{ec(pd)}$ in Eq. (4) are the phase space integrals and are functions of the stellar temperature (T), the density (ρ) and Fermi energy (E_f) of the electrons. They are explicitly given by

$$f_{ij}^{ec} = \int_{w_l}^{\infty} w\sqrt{w^2-1}(w_m + w)^2 F(+Z,w) G_- dw, \tag{7}$$

and by

$$f_{ij}^{pd} = \int_{1}^{w_m} w\sqrt{w^2-1}(w_m - w)^2 F(-Z,w)(1-G_+) dw. \tag{8}$$

In Eqs. (7) and (8), w is the total energy of the electron including its rest mass. w_m is the total β-decay energy,

$$w_m = m_p - m_d + E_i - E_j, \tag{9}$$

where m_p and E_i are masses and excitation energies of the parent nucleus, and m_d and E_j of the daughter nucleus, respectively. F($\pm$ Z,w) are the Fermi functions and were calculated according to the procedure adopted by Gove and Martin [55]. G$_\pm$ are the Fermi-Dirac distribution functions for positrons (electrons).

$$G_+ = \left[\exp\left(\frac{E+2+E_f}{kT}\right)+1\right]^{-1}, \tag{10}$$

$$G_- = \left[\exp\left(\frac{E-E_f}{kT}\right)+1\right]^{-1}, \tag{11}$$

here E is the kinetic energy of the electrons and k is the Boltzmann constant.

The total decay rate per unit time per nucleus was calculated using

$$\lambda^{ec(pd)} = \sum_{ij} P_i \lambda_{ij}^{ec(pd)}, \tag{12}$$

where P_i is the probability of the occupation of the parent excited states and follows the normal Boltzmann distribution. After the calculation of all partial rates for the transition $i \rightarrow j$ the summation was carried out over 200 initial (up to 10 MeV in parent nucleus) and 300 final states (up to 30 MeV in daughter nucleus) and satisfactory convergence was achieved in the rate calculation. The convergence was attributed to a spacious model space of $7\hbar\omega$

in our calculation. The excited states of an even-even nucleus in the current pn-QRPA model are two-proton and two-neutron quasiparticle states. On the other hand the daughter excited states are constructed as two-quasiparticle or four-quasiparticle states. Collective states cannot be calculated in the model and is a shortcoming of the current pn-QRPA model. In order to make up for this deficiency and to further increase the reliability of the calculated rates, experimental data were incorporated in the rate calculation wherever possible. The calculated excitation energies, using the pn-QRPA model, were replaced with measured levels when they were within 0.5 MeV of each other. Two missing 1^+ measured states in ^{60}Cu at 0.062 MeV and 0.346 MeV (along with their logft values of 5.33 and 5.93, respectively) were inserted manualy. No theoretical levels were replaced with the experimental ones beyond the excitation energy for which experimental compilations had no definite spin and/or parity.

4. Results and discussions

In the present application to the $A \sim 70$ region, one of the simplest form of IBM-1 Hamiltonian has been used and given as

$$\hat{H} = \epsilon\, \hat{n}_d + a_2\, \hat{Q} \cdot \hat{Q}. \tag{13}$$

Here, $\hat{n}_d$ and $\hat{Q}$ are the boson-number and quadrupole operators, respectively, defined in Eq. (2). It is to be noted that we have three parameters, ϵ, a_2, and $\overline{\chi}$ (in the quadrupole operator given in Eq. (2)).

The parametrization of the Hamiltonian constants was performed for the nuclei ^{60}Zn, ^{64}Ge, ^{68}Se, ^{72}Kr and ^{76}Sr located along the $N = Z$ line in the $A \sim 70$ mass region. Parameters were firstly fitted for the lightest ^{60}Zn nucleus and then later expanded up to ^{76}Sr, step by step.

The known energy levels in the ground state band of these nuclei were selected to fitted constant parameters of the Hamiltonian by minimizing the root-mean-square (*rms*) deviation. First, ϵ was adjusted and then a_2 by minimizing the *rms* deviation for each nucleus. Finally, same procedure was adopted for the $\overline{\chi}$ value for each nucleus. The determined parameters are given in Table 2. It can be seen from Table 2 that the $\overline{\chi}$ value of ^{72}Kr nucleus is higher than other $\overline{\chi}$ values. Detailed fitted procedure for $\overline{\chi}$ value was re-performed by keeping the same values for other two parameters (ϵ and a_2) and, as shown in Table 3, minimum *rms* was obtained at $\overline{\chi} = -1.3$. The subsequent results were sensible and shown in Fig. 1. In this figure, the energy ratio $R_{4/2} = E(4^+)/E(2^+)$ in the ground state band is illustrated for the studied nuclei along with typical values of the $U(5)$, $SU(3)$ and $O(6)$ symmetries. The ratio of the 4^+ and 2^+ yrast state energies indicates shape deformation in even-even nuclei and a smaller value of this ratio implies a less deformed nucleus [56]. It can be clearly seen from Fig. 1 that the $R_{4/2}$ values of ^{60}Zn, ^{64}Ge and ^{68}Se nuclei are almost same and located in between $U(5)$ and $O(6)$ symmetries and their fitted $\overline{\chi}$ values are also same. However the measured $R_{4/2}$ value of ^{72}Kr is smaller than 2.0 and positioned under the value of the $U(5)$ as its $\overline{\chi}$ value is quite different. The $R_{4/2}$ value of ^{76}Sr lies in between $O(6)$ and $SU(3)$ limits. The overall calculated results for low-lying energy spectra of given nuclei are displayed in Fig. 2. Experimental data were taken from the National Nuclear Data Center [57]. Using the simple IBM-1 model, we may infer that ^{60}Zn, ^{64}Ge, ^{68}Se and ^{72}Kr nuclei could be spherical since their energy ratios, illustrated in Fig. 1, are around 2.0 and are close to U(5). The $R_{4/2}$ value of ^{76}Sr is close to 3.33 and so this nucleus is axially deformed.

The experimentally known B(E2: $2_1^+ \rightarrow 0_1^+$) values of ^{68}Se and ^{72}Kr nuclei were also calculated using the boson effective charge $e_{\rm b} = 0.097\ eb$, fitted for $A \sim 100$ region given in Ref. [14], and $\overline{\chi}$ values given in Table 2. The calculated B(E2) values along with their comparison with experimental data, taken from the National Nuclear Data Center [57], are shown in Table 4.

As discussed above, the energy ratio is one of the important signatures for the geometric behavior of a given nucleus. However, other useful techniques include looking at the potential energy surface based on the coherent state formalism. For this work, the $V(\beta, \gamma)$ is reduced for the Hamiltonian as follows

$$V(\beta,\gamma) = \epsilon \frac{N\beta^2}{1+\beta^2} + a_2 N \left[\frac{5 + (1+\overline{\chi}^2)\beta^2}{1+\beta^2} + (N-1) \frac{\left(\frac{2\overline{\chi}^2\beta^4}{7} + 4\sqrt{\frac{2}{7}}\overline{\chi}\beta^3 \cos(3\gamma) + 4\beta^2 \right)}{(1+\beta^2)^2} \right] \tag{14}$$

The potential energy surfaces are illustrated in Fig. 3 for all nuclei included in the fit. As seen from the counterplot, the shapes of ^{60}Zn, ^{64}Ge, ^{68}Se, and ^{72}Kr are spherical but the shape of ^{76}Sr is deformed as also expected from the

signature of the energy ratio. As given in Table 1, $\beta_{IBM} = 0.86$ for ^{76}Sr. This value appears rather bigger but this result is reasonable for the IBM calculation since the SU(3) limit of β_{min} approaches $\sqrt{2}$ for large N [41]. According to the HFB calculation by using different interactions (e.g. Skyrme [23, 28], GognyD1S [24, 26], pairing-plus-quadrupole (P+Q) [25, 27]) for PESs in this region, ^{64}Ge is triaxial [23] or rigid triaxial [24], ^{68}Se is oblate [23], ^{72}Kr is oblate [23, 26] and ^{76}Sr is prolate [23].

We compare our calculated BGT$^+$ strength distribution for ^{60}Zn, ^{64}Ge and ^{68}Se against those calculated by Sarriguren [28] in Fig. 4. Details of the formalism of Sarriguren's calculation may be seen in [58, 59]. It is to be noted that Sarriguren used a quenching factor of 0.55 in his calculation. As mentioned earlier we incorporated a quenching factor of 0.6 in our calculation. Here the upper panels depict our calculation whereas the lower panels display the corresponding calculation by Sarriguren. The peak strengths in the daughter 1^+ states match well for the case of ^{64}Ge and ^{68}Se. We calculated a total BGT$^+$ strength of 5.08 (up to 10.8 MeV in daughter) for ^{60}Zn, 6.17 (up to 14.7 MeV in daughter) for ^{64}Ge and 5.73 (up to 14.4 MeV in daughter) for ^{68}Se. The corresponding strengths calculated by Sarriguren are 5.27, 5.03 and 4.96, respectively.

Experimental GT strength distribution for ^{72}Kr was studied at the ISOLDE PSB facility at CERN up to 3.3 MeV in ^{72}Br [60]. The measured GT strength distribution could only be established up to 2 MeV as only one additional level was established firmly at 3.3 MeV in ^{72}Br. Fig. 5 shows our calculated BGT$^+$ strength distribution for ^{72}Kr (upper panel). The middle panel shows the measured data and the bottom panel displays the Sarriguren calculation. The total strength calculated by Sarriguren up to 12.8 MeV in ^{72}Br is 4.56. This is to be compared with our calculated value of 4.96. Of special mention is the peak that we calculate at 3.3 MeV. The measured data also shows its peak at same excitation energy of 3.3 MeV in ^{72}Br.

The experimental GT strength distribution of the $N = Z$ nucleus ^{76}Sr was also studied at CER-ISOLDE [61]. We compare the experimental data with our calculation and those performed by Sarriguren in Fig. 6. Here we present the cumulative BGT$^+$ strength distribution. Sarriguren calculated a total strength of 5.07 up to 14.1 MeV to be compared with our value of 5.23. The experimental data bagged a total strength of 4.58.

The variation of the calculated half-lives verses the deformation parameter is shown in Fig. 7. Experimental half-lives are shown as black boxes whereas the calculated values are shown in circles. We varied the value of the deformation parameter β from -0.5 to 0.9 in our calculation. It can be seen from Fig. 7 that the calculated half-lives are sensitive function of the nuclear deformation parameter. Further the deformations from [47] reproduce well the measured half-lives of these $N = Z$ nuclei.

We compare our calculated half-lives for these neutron-deficient medium-mass WP nuclei with experimental and previous calculations in Fig. 8. Experimental half-lives were taken from the recent atomic mass evaluation AME2012 [48]. Shown also in Fig. 8 are the Hartree-Fock (HF) and QRPA calculations using the Sk3 [62] and SG2 [63] forces performed by Sarriguren and collaborators [64]. Biehle and Vogel [65] also performed a QRPA calculation for ^{76}Sr, which is in very good agreement with measured half-life, and is also shown in Fig. 8. It is noted that HF half-lives are systematically lower than the corresponding QRPA and experimental values. It is well known fact that the QRPA correlations tend to reduce the mean-field Gamow-Teller strength thereby increasing the calculated half-life values. We calculated a half-life of 152.3 s for ^{60}Zn to be compared with the experimental value of 142.8 s. Other models did not calculate half-life of ^{60}Zn. Our calculated half-lives are in good agreement with experimental values. Our calculated percentage deviation from measured values for ^{60}Zn, ^{64}Ge, ^{68}Se, ^{72}Kr and ^{76}Sr are 6.7%, 10.5%, 9.7%, 6.8% and 1.0%, respectively.

The current pn-QRPA model was used earlier to calculate rp-process weak-interaction mediated rates of waiting-point nuclei [49] but using different model parameters discussed earlier. Figs. 9 to 13 show the calculated weak-interaction mediated rates for the WP nuclei as a function of the stellar temperature and the density. The left-panels of these figures show the stellar electron capture (cEC) and positron decay (β^+) rates as a function of the stellar temperature for selected density of 10^5, 10^6, $10^{6.5}$ and 10^7 g.cm^{-3} (pertinent to rp-process conditions). The positron decay rates remain constant as the stellar density increases by two orders of the magnitude. The right panels show the total sum of these two rates. The upper panels are the Skyrme HF+BCS+QRPA calculation of Sarriguren and reproduced from [28] whereas the lower panels depict our results. Sarriguren calculated his rates only up to stellar temperature of 10 GK. We performed our calculation up to 30 GK. The shaded region is the temperature range considered to be most relevant with the rp-process [28]. Fig. 9 shows the comparison of the stellar rates for ^{60}Zn. It can be noted that our positron decay rates are around a factor 3 less than Sarriguren rates under rp-process conditions. At temperatures of 10 GK our positron decay rates are factor 6 bigger. Our calculated electron capture rates are in

reasonable comparison with Sarriguren calculation for rp-process conditions. Our calculated total rates are factor 2 smaller for rp-process temperatures at density (10^4 - 10^5) g.cm^{-3} and in very good agreement with Sarriguren calculated total rates at density(10^6 - 10^7) g.cm^{-3}. Another feature to be noted is that for rp-process conditions, our calculated positron decay rates are factor (1 – 6) bigger at $\rho = 10^5$ gm.cm^{-3} when compared with our calculated electron capture rates. However as stellar density reaches $\rho = 10^7$ gm.cm^{-3}, the calculated electron capture rates increases and are factor (16 – 19) bigger than the competing positron decay rates.

Fig. 10 shows comparison of the stellar weak rates for ^{64}Ge. Here we note that our electron capture and positron decay rates are in good agreement with Sarriguren rates for rp-process conditions. At high temperature of 10 GK our electron capture (positron decay) rates are factor 2 (5) bigger. Our calculated positron capture rates are up to factor 20 (2) bigger than the electron capture rates at $\rho = 10^5$ (10^6) gm.cm^{-3} for rp-process temperature range and are factor 4 smaller at $\rho = 10^7$ gm.cm^{-3}.

For the case of ^{68}Se, Fig. 11 shows that our rates are up to three times bigger the corresponding Sarriguren rates for rp-process conditions. At soaring temperatures around 10 GK our positron decay rates are up to an order of the magnitude bigger whereas the calculated electron capture rates are factor 4 bigger. Once again our calculated electron capture rates are factor (7 – 8) bigger than the competing pn-QRPA positron decay rates at $\rho = 10^7$ gm.cm^{-3} and T = 1 – 3 GK.

Comparison of the electron capture rates under rp-process conditions for the case of ^{72}Kr is almost perfect (see Fig. 12). Our calculated positron decay rates are half those calculated by Sarriguren under similar physical conditions. At high temperatures our positron decay rates are factor 5 bigger. For rp-process conditions, the pn-QRPA calculated electron capture rates are same as the β^+ decay rates at $\rho = 10^6$ gm.cm^{-3}. At higher stellar density of $\rho = 10^7$ gm.cm^{-3}, the calculated electron capture rates are an order of the magnitude bigger.

Fig. 13 finally shows that for the prolate nucleus ^{76}Sr, Sarriguren calculated rates are in perfect agreement with our calculation under rp-process conditions. At high temperatures our positron decay (electron capture) rates are factor 18 (2) bigger. For rp-process temperatures, our calculated positron decay rates is factor 3 bigger at a stellar density of 10^6 gm.cm^{-3} compared to our electron capture rates. When the density increases by an order of the magnitude our electron capture rates are three times the calculated β^+ decay rates.

Figs. 9 to 13 show that our calculated rates are enhanced at high temperatures as compared to the Skyrme HF+BCS+QRPA calculation. At high temperatures the calculated electron capture rates are more than an order of magnitude bigger in comparison with the competing positron decay rates. Convergence of the rate calculation is in order as temperature increases to 10 GK and beyond (see Eq. (12)) due to finite occupation probability of parent excited states. We took 200 initial and 300 final states in our rate calculation which guaranteed satisfactory convergence in our rate calculation. We note that due to the availability of a huge model space (up to 7 major oscillator shells) in our pn-QRPA model, convergence was achieved in our rate calculations for excitation energies well in excess of 10 MeV. On the other hand the self-consistent approach of the Skyrme HF+BCS+QRPA calculation forces one to use limited configuration spaces which might lead to convergence problem in rate calculation. Table 5 shows the excited states contribution to the total electron capture and positron decay rates under stellar conditions. It is noted that as stellar temperature soars to 30 GK, a sizeable contribution comes from the excited states. The excited states contribution is around two orders of magnitude bigger for positron decay rates when compared with the corresponding stellar electron capture rates. The table also shows that under rp-process conditions the contributions from excited states are almost negligible.

5. Conclusions

Accurate estimate of the positron decay and electron capture rates of the WP neutron-deficient medium mass nuclei are required for a better understanding of the rp-process. Incidently nuclear deformation is believed to play a crucial role in determining the strength distributions of the β-decay for these medium mass nuclei. Besides there exist a wide variety of the nuclear shapes displayed in this region. In this project we selected five, $N = Z$, the WP nuclei, namely ^{60}Zn, ^{64}Ge, ^{68}Se, ^{72}Kr and ^{76}Sr, to study their nuclear structure properties and geometric shapes and to calculate their half-lives and associated stellar weak rates. The nuclear shape was determined using the PES of the IBM-1 model. The model calculated essentially spherical nuclei for the first four cases and a β_{min} value of 0.86 for ^{76}Sr. As we were not able to find in literature an exact formula to convert our IBM calculated β to deformations for

use in Nilsson model, we decided to use the deformations calculated from the relativistic mean-field theory. We then performed a pn-QRPA calculation in a huge model space of $7\hbar\omega$ to calculate the half-lives of these neutron-deficient WP nuclei. The calculated half-lives were in very good agreement with the experimental half-lives determined from the recent atomic mass evaluation AME2012.

We presented the BGT strength distribution for the WP nuclei and compared with previous calculation and measurements wherever possible. Our calculated strength was in decent comparison with the measured data. For the case of ^{60}Zn, the Skyrme HF+BCS+QRPA calculation of total GT strength, performed by Sarriguren, was slightly bigger. For remaining cases our calculated total GT strength was bigger. Our calculated total strength was in good comparison with Sarriguren calculation for the case of ^{60}Zn and ^{76}Sr. We then calculated the positron decay and electron capture rates for these proton rich WP nuclei in stellar matter with special focus on rp-process conditions. Our stellar rates were also compared with those performed by Sarriguren and agreed to within a factor of two for rp-process conditions.

Our calculation showed that electron capture rates compete well with the positron decay rates under rp-process conditions. In essence the electron capture rates were bigger, by more than an order of the magnitude, than the competing β^+ decay rates for temperature of 3 GK and density $\rho = 10^7$ gm.cm^{-3}. Our findings reiterates the fact that electron capture rates on WP proton-rich nuclei form an integral part of the weak rates under rp-process conditions and must not be neglected in nuclear network calculations.

Acknowledgements

J.-U. Nabi wishes to acknowledge the support provided by the Higher Education Commission (Pakistan) through the HEC Project No. 20-3099.

References

[1] H. Schatz, et al., Phys. Rep. 294 (1998) 167.
[2] R. K. Wallace and S. E. Woosley, Ap. J. Suppl. Ser. 45 (1981) 389.
[3] D. Prialnik, *An Introduction to the theory of stellar structure and evolution* (Cambridge University Press, Cambridge, 2000).
[4] L. Van Wormer, J. Görres, C. Iliadis, M. Wiescher and F.-K. Thielemann, Astrophys. J. 432 (1994) 326.
[5] H. Schatz, et al., Phys. Rev. Lett. 86 (2001) 3471.
[6] A. Arima and F. Iachello, Phys. Rev. Lett. 35 (1975) 1069.
[7] A. Arima and F. Iachello, Ann. Phys. (N.Y.) 99 (1976) 253.
[8] A. Arima and F. Iachello, Ann. Phys. (N.Y.) 111 (1978) 201.
[9] A. Arima and F. Iachello, Ann. Phys. (N.Y.) 123 (1979) 468.
[10] K. A. Gladnishki, et al., Nucl. Phys. A 877 (2012) 19.
[11] M. Albers, et al., Nucl. Phys. A 899 (2013) 1.
[12] H. Duckwitz, et al., Nucl. Phys. A 903 (2013) 18.
[13] T. Thomas, et al., Phys. Rev. C 88, (2013) 044305.
[14] M. Böyükata, P. Van Isacker and İ. Uluer, J. Phys. G: Nucl. Part. Phys. 37, (2010) 105102.
[15] K. Nomura, T. Otsuka, N. Shimizu, and L. Guo, Phys. Rev. C 83, 041302(R) (2011) 041302(R).
[16] K. Nomura, et al., Phys. Rev. C 84 (2011) 054316.
[17] K. Nomura, et al., Phys. Rev. C 83 (2011) 054303.
[18] J. E. García-Ramos,and K. Heyde, Phys. Rev. C 89 (2014) 014306.
[19] J. E. García-Ramos, et al., Phys. Rev. C 89 (2014) 014313.
[20] J. Kotila and S. M. Lenzi, Phys. Rev. C 89 (2014) 064304.
[21] S. T. Hsieh, H. C. Chiang and Der-San Chuu Phys. Rev. C 46 (1992) 195.
[22] A. Giannatiempo, P. Sona and A. Nannini Phys. Rev. C 62 (2000) 044302.
[23] M. Yamagami, K. Matsuyanagi and M.Matsuob Nuclear Physics A 693 (2001) 579
[24] A. Corsi, et al., Phys. Rev. C 88 (2013) 044311.
[25] M. Kobayasi, T. Nakatsukasa, M. Matsuo and K. Matsuyanagi, Eur. Phys. J. A 25 (2005) 01.
[26] M. Girod, J. P. Delarochea, A. Gorgenb, A. Obertelli, Phys. Lett. B 676 (2009) 39.
[27] N. Hinohara, K. Sato, T. Nakatsukasa, M. Matsuo and K. Matsuyanagi, Phys. Rev. C 82 (2010) 064313.
[28] P. Sarriguren, Phys. Rev. C 83 (2011) 025801.
[29] A. Staudt, E. Bender, K. Muto and H. V. Klapdor-Kleingrothaus, At. Data Nucl. Data Tables 44 (1990) 79.
[30] M. Hirsch, A. Staudt, K. Muto and H. V. Klapdor-Kleingrothaus, At. Data Nucl. Data Tables 53 (1993) 165.
[31] J.-U. Nabi and H. V. Klapdor-Kleingrothaus, Eur. Phys. J. A 5 (1999) 337.
[32] I. Talmi, *Simple Models of Complex Nuclei: The Shell Model and The Interacting Boson Model (Contemporary Concepts in Physics, Volume 7)* (Harwood Academic Publishers, 1993).

[33] A. Arima, T. Otsuka, F. Iachello, and I. Talmi, Phys. Lett. B 66 (1977) 205.
[34] T. Otsuka, A. Arima, F. Iachello, and I. Talmi, Phys. Lett. B 76 (1978) 139.
[35] A. Arima, T. Otsuka, and F. Iachello, Nucl. Phys. A 309 (1978) 1.
[36] R. F. Casten and D. D. Warner, Rev. Mod. Phys. 60 (1988) 389.
[37] F. Iachello and A. Arima, *The Interacting Boson Model* (Cambridge University Press, Cambridge, 1987).
[38] A. Bohr and B. R. Mottelson, *Nuclear Structure. Volume 2: Nuclear Deformation*, (World Scientific Publishing, 1998).
[39] A. E. L. Dieperink, O. Scholten and F. Iachello, Phys. Rev. Lett. 44 (1980) 1747.
[40] A. E. L. Dieperink and O. Scholten, Nucl. Phys. A 346 (1980) 125.
[41] J. N. Ginocchio and M. W. Kirson, Phys. Rev. Lett. 44 (1980) 1744.
[42] J. N. Ginocchio and M. W. Kirson, Nucl. Phys. A 350 (1980) 31.
[43] P. Van Isacker and J.Q. Chen, Phys. Rev. C 24 (1981) 684.
[44] S. G. Nilsson, Mat. Fys. Medd. Dan. Vid. Selsk 29 (1955) 16.
[45] K. Nomura, N. Shimizu and T. Otsuka, Phys. Rev. C 81 (2010) 044307.
[46] I. Stetcu and C. W. Johnson C.W., Phys. Rev. C 69 (2004) 024311.
[47] G. A. Lalazissiz, S. Raman and P. Ring, At. Data Nucl. Data Tables 71 (1999) 1.
[48] G. Audi, et al., Chin. Phys. C 36 (2012) 1287; M. Wang, et al., Chin. Phys. C 36 (2012) 1603.
[49] J.-U. Nabi, Astrophys. Space Sci. 339 (2012) 305.
[50] P. Möller and J. R. Nix,. At. Data Nucl. Data Tables 26 (1981) 165.
[51] G. P. Yost, et al. (Particle Data Group), Phys. Lett. B 204 (1988) 1.
[52] V. Rodin, A. Faessler and F. Simkovic, P. Vogel, Czech. J. Phys. 56 (2006) 495.
[53] J.-U. Nabi and H. V. Klapdor-Kleingrothaus, At. Data Nucl. Data Tables 71 (1999) 149.
[54] J.-U. Nabi and H. V. Klapdor-Kleingrothaus, At. Data Nucl. Data Tables 88 (2004) 237.
[55] N. B. Gove and M. J. Martin, At. Data Nucl. Data Tables 10 (1971) 205.
[56] R. F. Casten, N. V. Zamfir and D. S. Brenner, Phys. Rev. Lett. 71 (1993) 227.
[57] National Nuclear Data Center (NNDC), http://www.nndc.bnl.gov/ (2014).
[58] P. Sarriguren, Phys. Rev. C 79 (2009) 044315.
[59] P. Sarriguren, Phys. Lett. B 680 (2009) 438.
[60] I. Piqueras, et al., Eur. Phys. J. A 16 (2003) 313.
[61] E. Nácher, et al., Phys. Rev. Lett. 92 (2004) 232501.
[62] M. Beiner, H. Flocard, N. Van Giai and P. Quentin, Nucl. Phys. A 238 (1975) 29.
[63] N. Van Giai and H. Sagawa, Phys. Lett B 106 (1981) 379.
[64] P. Sarriguren, R. Alvarez-Rodriguez and E. Moya de Guerra, Eur. Phys. J. A 24 (2005) 193.
[65] G. T. Biehle and P. Vogel, Phys. Rev. C 46 (1992) 1555.

Nucelus	^{60}Zn	^{64}Ge	^{68}Se	^{72}Kr	^{76}Sr
N	2	4	6	8	10
β[IBM]	0	0	0	0	0.86
β [47]	+0.170	+0.217	-0.285	-0.358	+0.410

Table 1. Calculated values of nuclear deformation using the IBM-1 Model and those using the relativistic mean-field theory [47]. N is boson number.

	N	$\epsilon^{[1]}$	$a_2^{[1]}$	$\overline{\chi}^{[2]}$	$\sigma^{[3]}$
^{60}Zn	2	883	-52.3	-0.35	0
^{64}Ge	4	914.1	-77.2	-0.35	15
^{68}Se	6	1116.8	-59.8	-0.35	12
^{72}Kr	8	1026.85	-26.4	-1.3	60
^{76}Sr	10	300.6	-71.1	-0.25	4

Table 2. The fitted parameters of the IBM-1 Hamiltonian (Eq. 1). [1] given in units of keV, [2] dimensionless, [3] the root-mean-square (*rms*) deviation in units of keV.

$\overline{\chi}$	-0.2	-0.4	-0.6	-0.7	-0.8	-0.9	-1.0	-1.1	-1.2	-1.
σ	69	68	67	66	65	64	63	62	61	60

Table 3. Detail fitted procedure for $\overline{\chi}$ value of ^{72}Kr nucleus.

	Exp.	IBM-1
^{60}Zn	-	2.04
^{64}Ge	-	5.26
^{68}Se	4.45 (0.66)	8.94
^{72}Kr	10.14 (1.42)	12.41
^{76}Sr	-	25.68

Table 4. Experimental and calculated B(E2: $2_1^+ \rightarrow 0_1^+$) values in units of 10^{-2} e^2b^2

		^{60}**Zn**		
$(\rho, \mathbf{T_9})$	$\lambda_{\mathbf{ec}}(\mathbf{G})$	$\mathbf{R_{ec}(G/T)}$	$\lambda_{\mathbf{pd}}(\mathbf{G})$	$\mathbf{R_{pd}(G/T)}$
($10^{6.5}$,1)	2.32E-02	1.00E+00	4.87E-03	1.00E+00
($10^{6.5}$,1.5)	2.39E-02	1.00E+00	4.87E-03	1.00E+00
($10^{6.5}$,2)	2.49E-02	1.00E+00	4.87E-03	1.00E+00
($10^{6.5}$,2.5)	2.62E-02	1.00E+00	4.87E-03	1.00E+00
($10^{6.5}$,3)	2.80E-02	1.00E+00	4.87E-03	9.98E-01
($10^{6.5}$,30)	7.65E+00	4.65E-02	2.11E-04	2.29E-04
		^{64}**Ge**		
($10^{6.5}$,1)	1.08E-02	1.00E+00	7.81E-03	1.00E+00
($10^{6.5}$,1.5)	1.10E-02	1.00E+00	7.81E-03	1.00E+00
($10^{6.5}$,2)	1.12E-02	1.00E+00	7.81E-03	1.00E+00
($10^{6.5}$,2.5)	1.14E-02	1.00E+00	7.81E-03	1.00E+00
($10^{6.5}$,3)	1.15E-02	1.00E+00	7.81E-03	9.96E-01
($10^{6.5}$,30)	6.69E+00	3.52E-02	2.96E-04	5.44E-04
		^{68}**Se**		
($10^{6.5}$,1)	3.63E-02	1.00E+00	1.68E-02	1.00E+00
($10^{6.5}$,1.5)	3.68E-02	1.00E+00	1.68E-02	1.00E+00
($10^{6.5}$,2)	3.75E-02	1.00E+00	1.68E-02	1.00E+00
($10^{6.5}$,2.5)	3.87E-02	1.00E+00	1.68E-02	1.00E+00
($10^{6.5}$,3)	4.05E-02	1.00E+00	1.68E-02	9.99E-01
($10^{6.5}$,30)	9.35E+00	4.95E-02	7.70E-04	6.56E-04
		^{72}**Kr**		
($10^{6.5}$,1)	4.99E-02	1.00E+00	1.63E-02	1.00E+00
($10^{6.5}$,1.5)	5.05E-02	1.00E+00	1.63E-02	1.00E+00
($10^{6.5}$,2)	5.14E-02	1.00E+00	1.63E-02	1.00E+00
($10^{6.5}$,2.5)	5.28E-02	1.00E+00	1.63E-02	1.00E+00
($10^{6.5}$,3)	5.52E-02	1.00E+00	1.63E-02	9.99E-01
($10^{6.5}$,30)	9.18E+00	4.08E-02	6.94E-04	3.51E-04
		^{76}**Sr**		
($10^{6.5}$,1)	1.05E-01	1.00E+00	1.14E-01	1.00E+00
($10^{6.5}$,1.5)	1.06E-01	1.00E+00	1.14E-01	1.00E+00
($10^{6.5}$,2)	1.07E-01	1.00E+00	1.14E-01	1.00E+00
($10^{6.5}$,2.5)	1.09E-01	1.00E+00	1.14E-01	1.00E+00
($10^{6.5}$,3)	1.13E-01	1.00E+00	1.14E-01	9.99E-01
($10^{6.5}$,30)	1.18E+01	2.64E-02	5.02E-03	5.75E-04

Table 5. The *ground state* electron and positron decay rates, $\lambda_{ec}(G)$, $\lambda_{pd}(G)$, respectively, for ^{60}Zn, ^{64}Ge, ^{68}Se, ^{72}Kr and ^{76}Sr in units of sec^{-1}. Given also are the ratios of the ground state capture and decay rates to total rate, $R_{ec}(G/T)$, $R_{pd}(G/T)$, respectively. The first column gives the corresponding values of stellar density, ρ (gcm^{-3}), and temperature, T_9 (in units of 10^9 K), respectively.

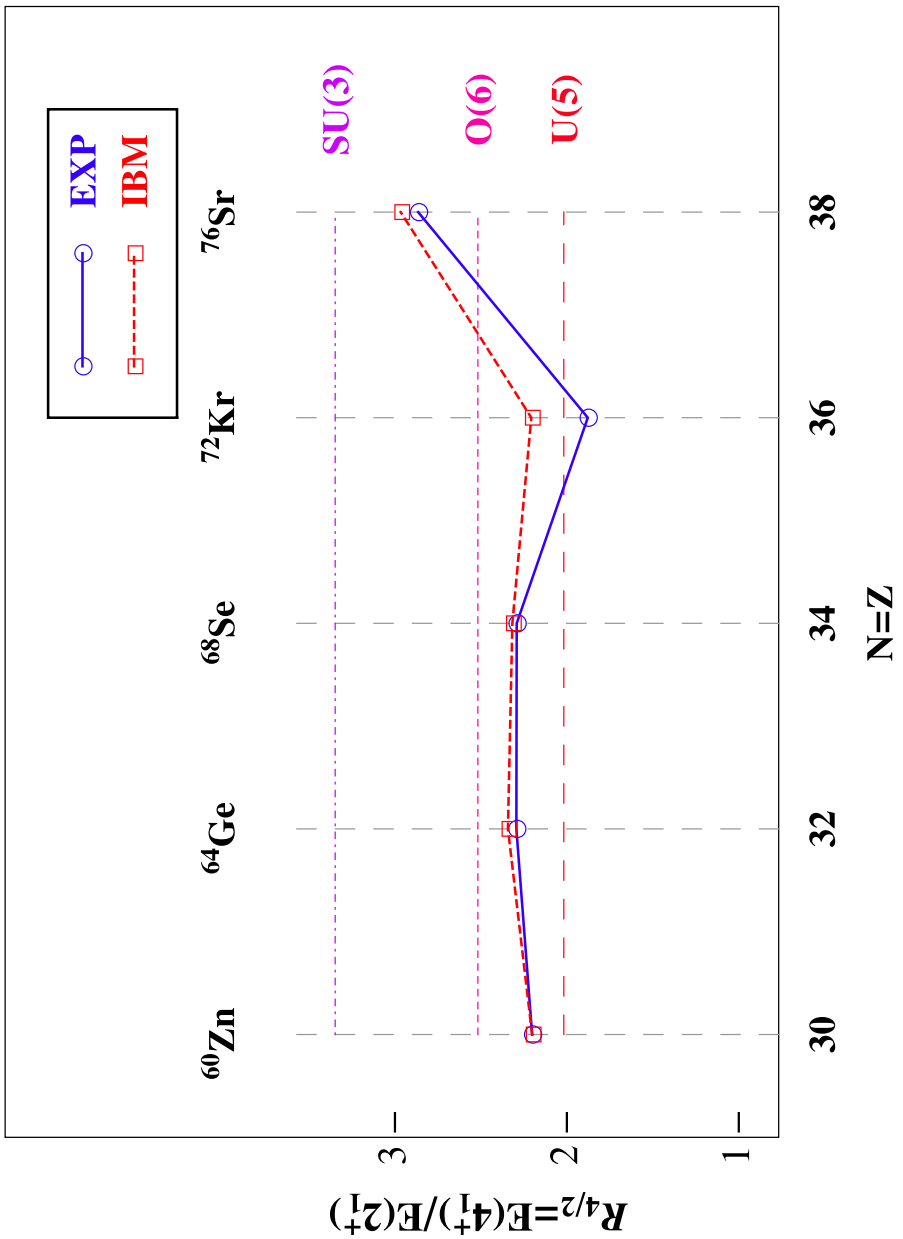

Figure 1. (Color online) Values of the energy ratio $R_{4/2} = E(4^+_1)/E(2^+_1)$ for $N = Z$ nuclei.

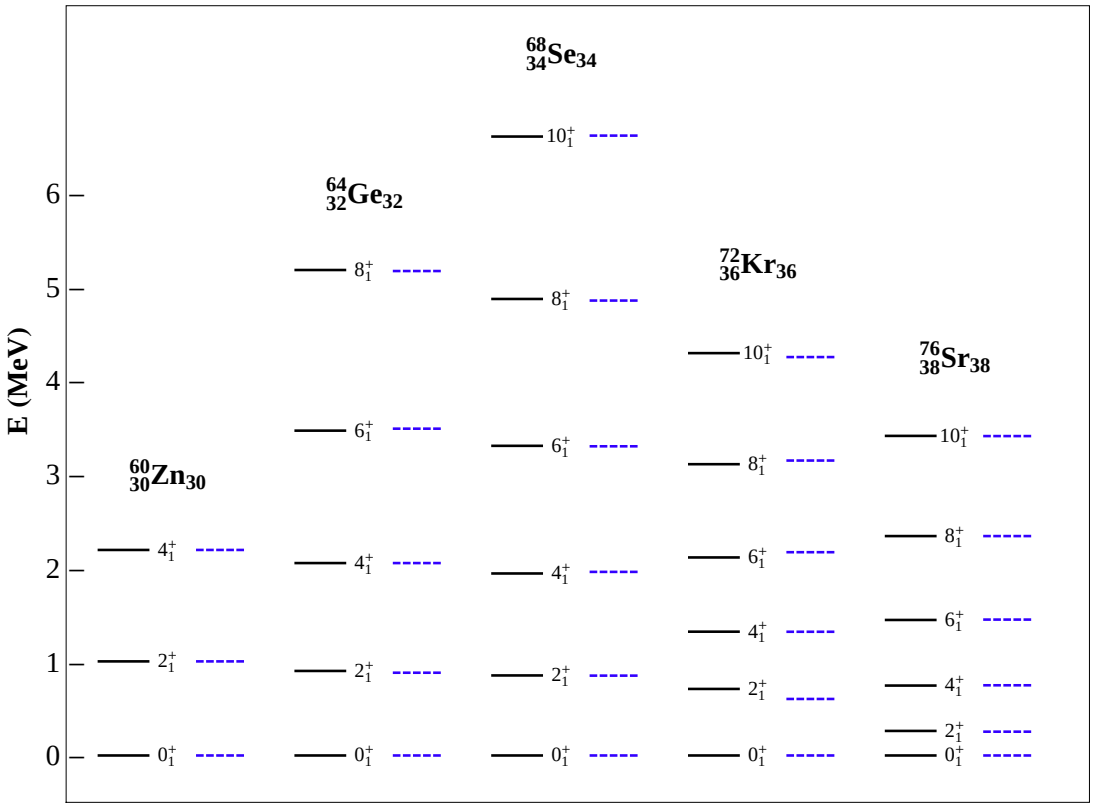

Figure 2. (Color online) The experimental (straight lines) and calculated (dashed lines) energy spectra for ground-state bands of ^{60}Zn, ^{64}Ge, ^{68}Se, ^{72}Kr and ^{76}Sr nuclei.

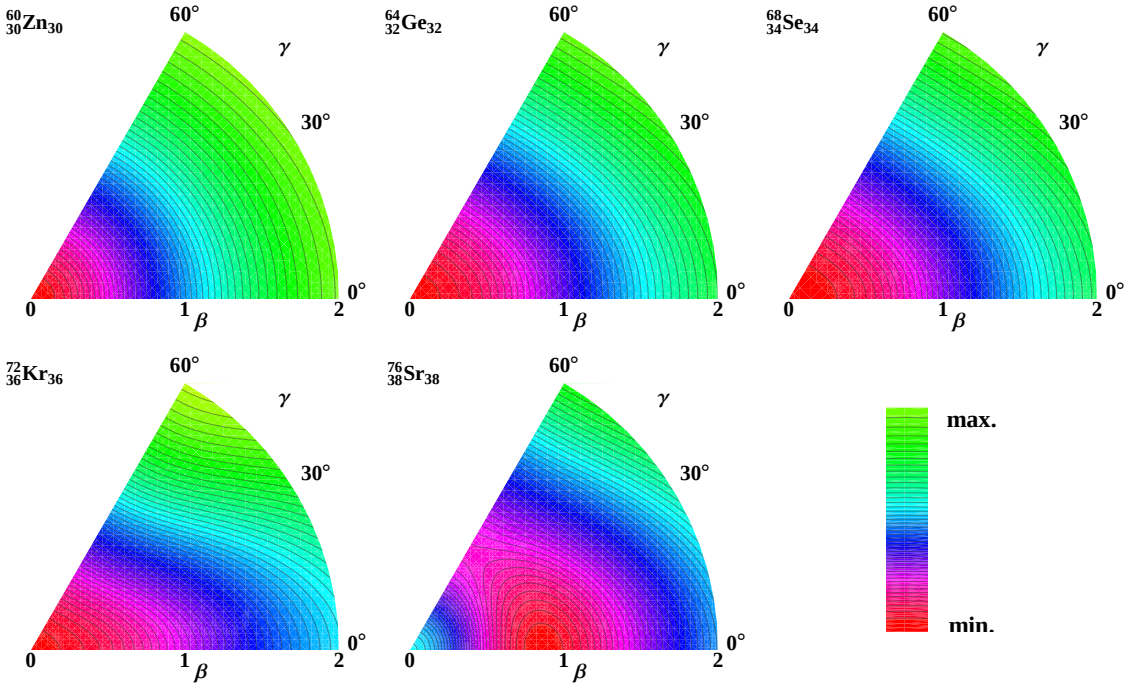

Figure 3. (Color online) Potential energy surfaces for ^{60}Zn, ^{64}Ge, ^{68}Se, ^{72}Kr and ^{76}Sr nuclei.

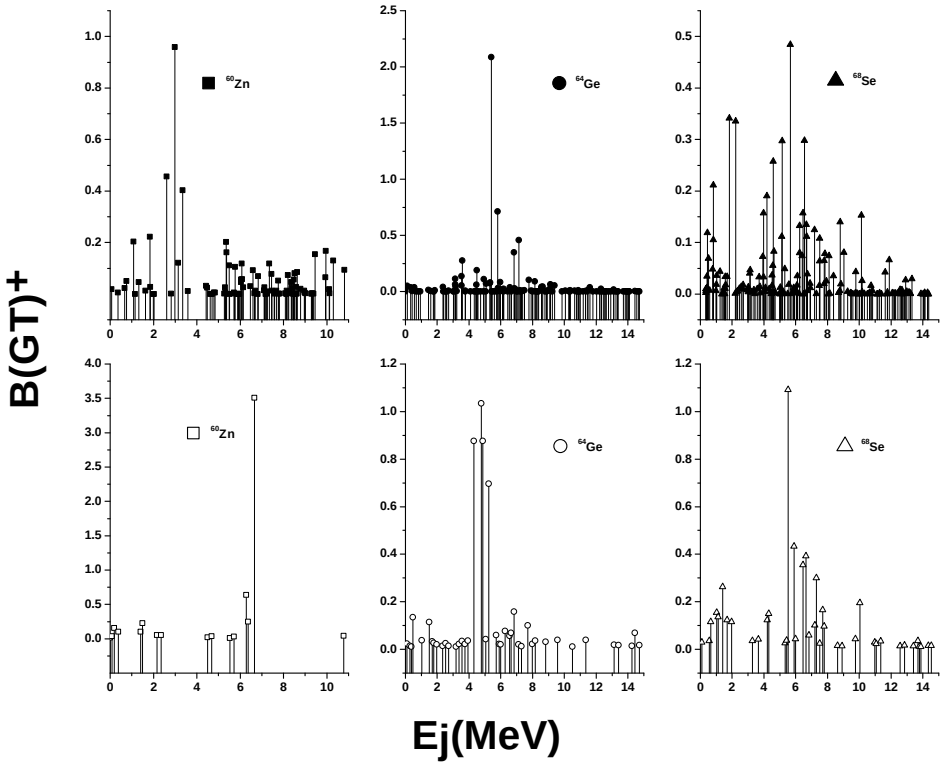

Figure 4. Calculated BGT$^+$ strength distribution for ^{60}Zn, ^{64}Ge and ^{68}Se. Upper panels show calculation of this work and lower panels those performed by Sarriguren [28].

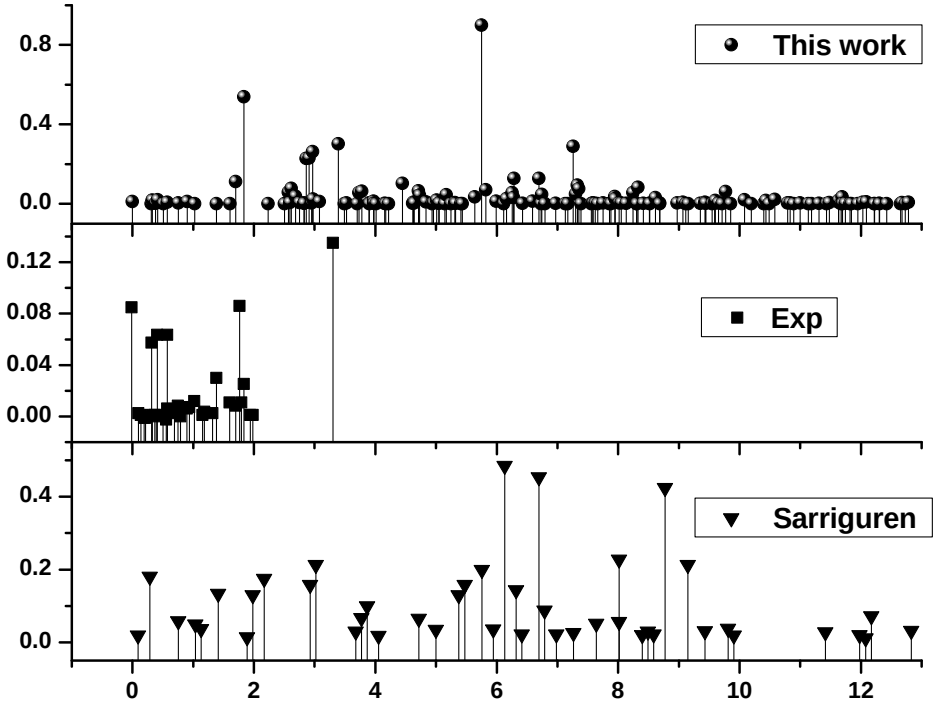

Figure 5. BGT^{+} strength distribution for ^{72}Kr. Experimental data taken from [60]. Lower panel shows calculation by [28].

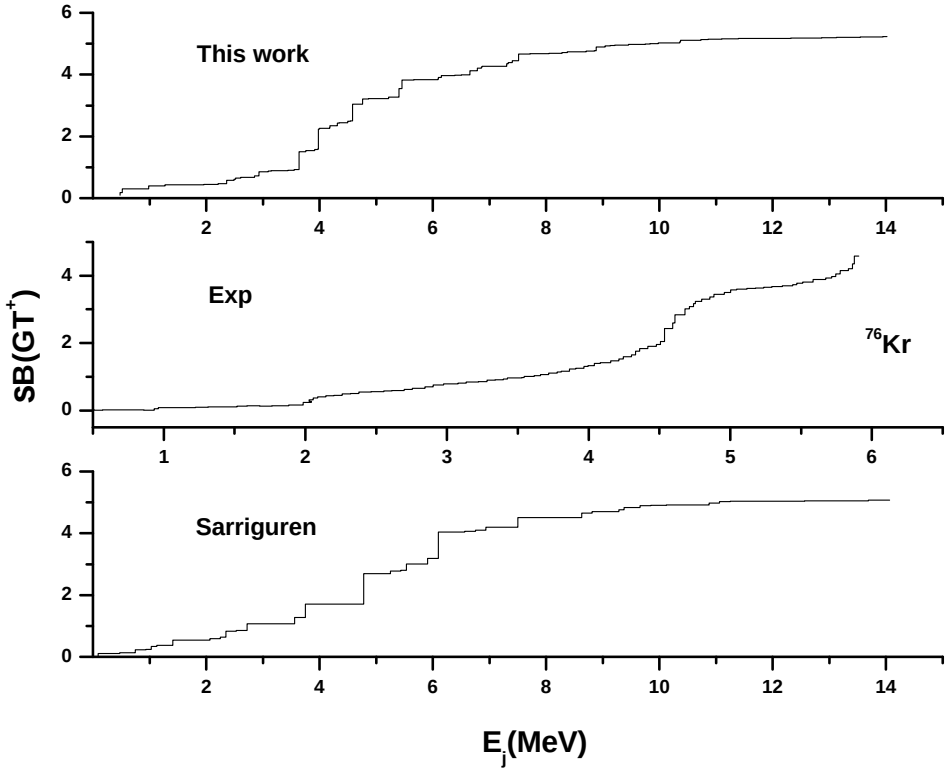

Figure 6. Cumulative BGT$^+$ strength distribution for ^{76}Sr. Experimental data taken from [61]. Lower panel shows calculation by [28].

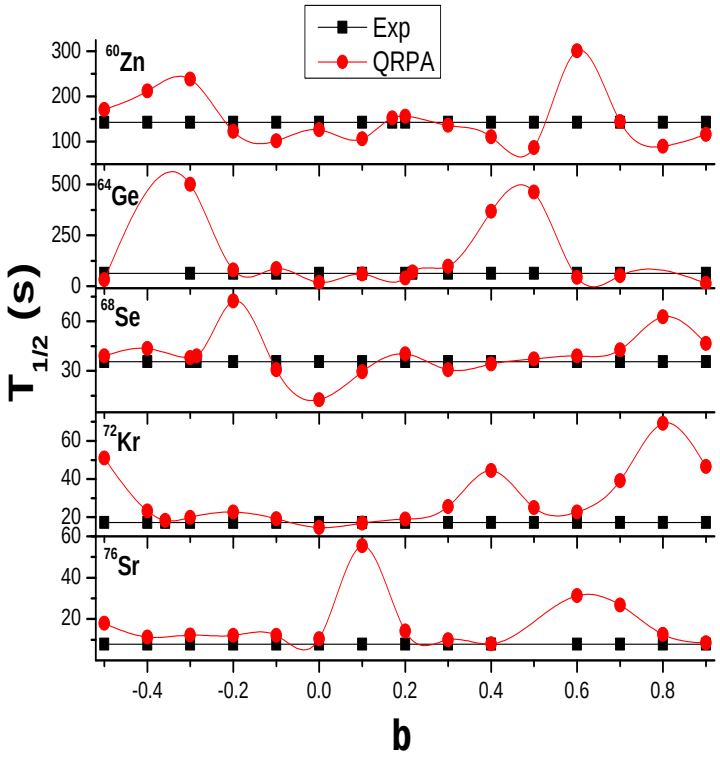

Figure 7. Dependence of calculated half-lives on the values of deformation parameter for $N = Z$ nuclei.

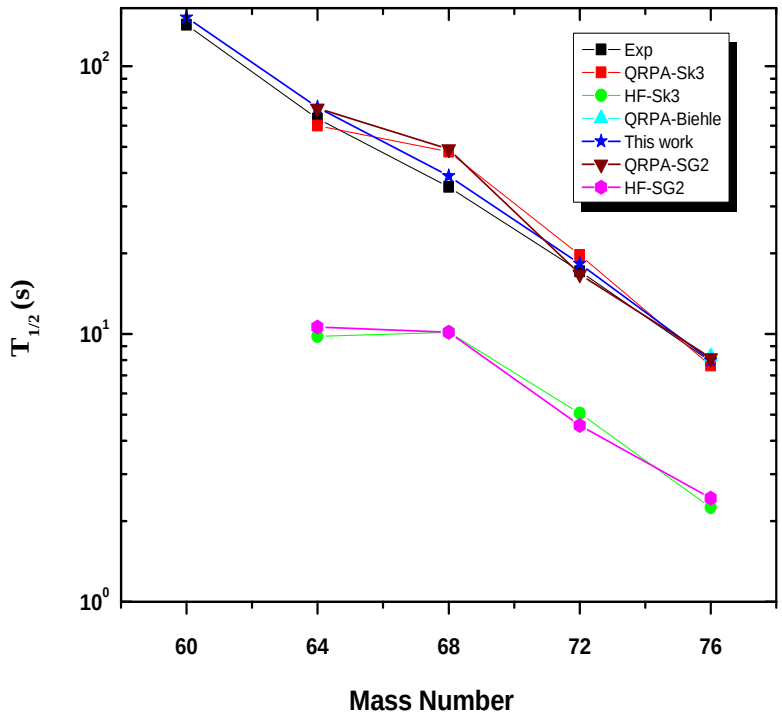

Figure 8. (Color online) Comparison of experimental half-lives for WP nuclei with this work and previous calculations.

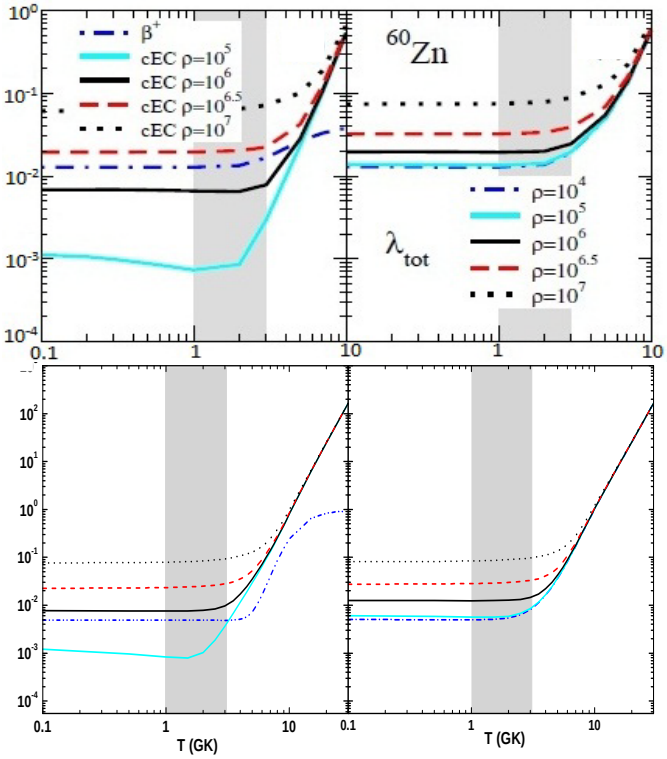

Figure 9. (Color online) Comparison of calculated weak-interaction mediated rates for ^{60}Zn as a function of stellar temperature and density. The upper panels show the deformed Skyrme Hartree-Fock + BCS + QRPA calculation reproduced from [28]. The bottom panels show the reported pn-QRPA calculation. The left panels show the electron capture and positron decay rates whereas the right panels show the combined total rates. All rates are given in units of s^{-1}. Densities are given in units of gcm^{-3} and temperatures in units of 10^9 K.

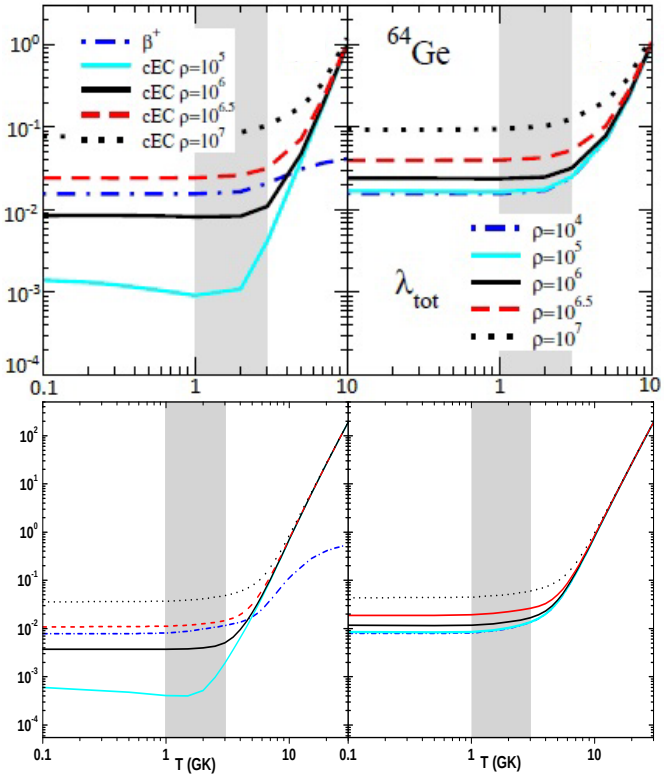

Figure 10. (Color online) Same as Fig. 9 but for ^{64}Ge.

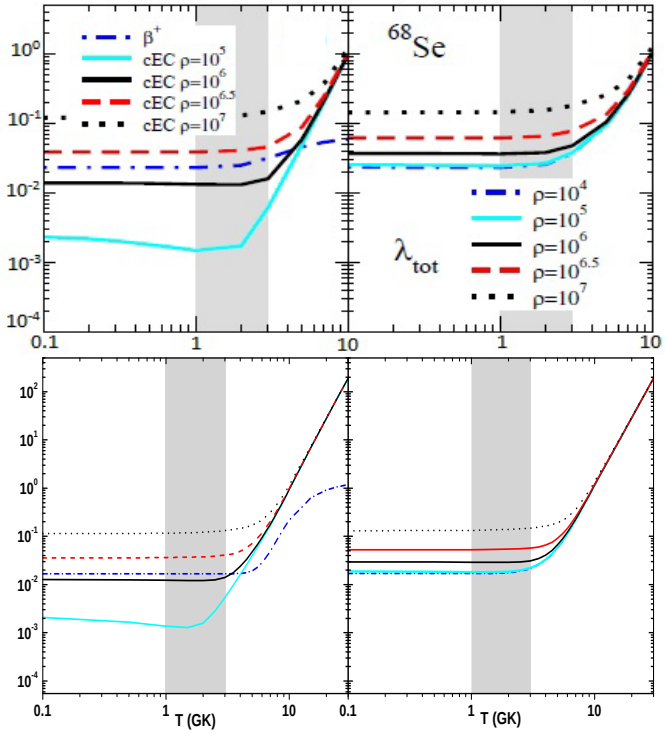

Figure 11. (Color online) Same as Fig. 9 but for ^{68}Se.

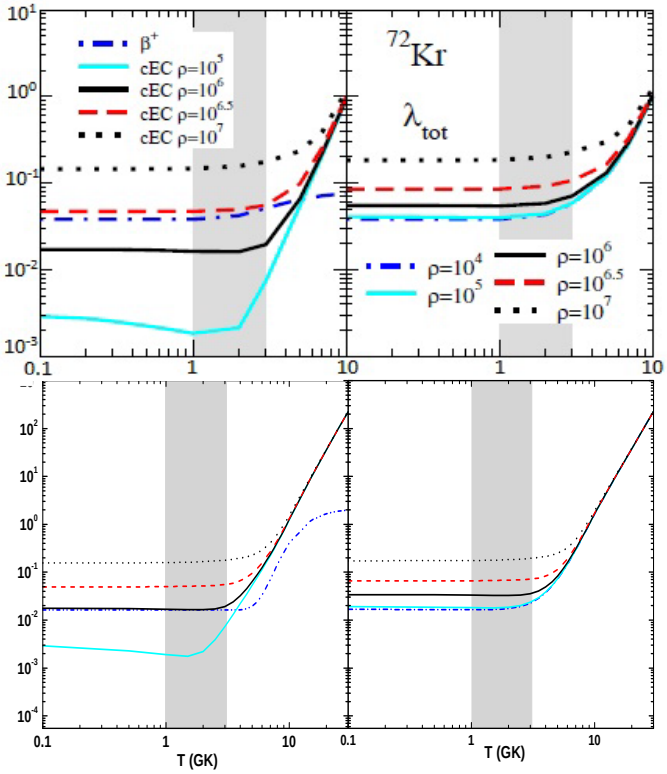

Figure 12. (Color online) Same as Fig. 9 but for ^{72}Kr.

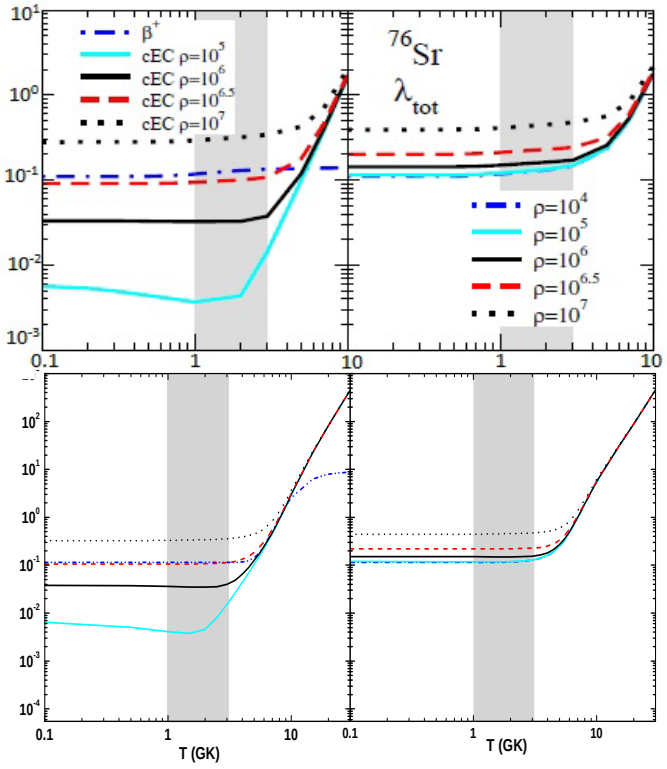

Figure 13. (Color online) Same as Fig. 9 but for ^{76}Sr.